Experimental and numerical thermo-mechanical analysis of wire-based laser metal deposition of Al-Mg alloys

Bock, Frederic E.; Herrnring, Jan; Froend, Martin; Enz, Josephin; Kashaev, Nikolai; Klusemann, Benjamin

Experimental and numerical thermo-mechanical analysis of wire-based laser metal deposition of Al-Mg alloys

Frederic E. Bock [a],[*], Jan Herrnring [a], Martin Froend [a], Josephin Enz [a], Nikolai Kashaev [a], Benjamin Klusemann [a],[b]

[a] Institute of Materials Mechanics, Helmholtz-Zentrum Geesthacht, Max-Planck-Strasse 1, D-21502 Geesthacht, Germany
[b] Institute of Product and Process Innovation, Leuphana University of Lüneburg, Universitätsallee 1, D-21335 Lüneburg, Germany

A R T I C L E   I N F O

A B S T R A C T

A finite element model is employed to perform a sequentially coupled thermo-mechanical analysis for enabling rapid process simulations of temperature fields, residual stresses and distortions for the production of additively manufactured parts via laser metal deposition. Experimental identification of characteristic process features such as temperature distribution, melt pool dimensions and bead geometries were used for the initial built-up and calibration of the model. The addition of material during process simulation is realised through reactivating inactive elements during the transient heat transfer analysis and through reactivating a combination of inactive and quiet elements during the mechanical analysis. The travelling heat source is geometrically bounded to precisely control the volume of its energy distribution. The results of the transient heat transfer analysis are sequentially coupled to a mechanical analysis for obtaining information on the resulting residual stresses and deformation. Based on the good agreement between numerical and experimental results of the thermal analysis, conclusions on the corresponding residual stress distributions and deformation are made. It is shown that the model represents an efficient tool for process prediction regarding thermal history, residual stresses and final-part deformations. Finally, the model is utilised to identify parameters and conditions of the process that lead to reduced residual stresses and deformations of the investigated additive part.

1. Introduction

The increasing industrial and societal demand for minimising fossil fuel consumption enforces the need to utilise weight saving strategies in transportation industries [1]. The popularity of additive manufacturing (AM) has been on a continuous surge in both research and industry in the past decades [2]. Major drivers are efficient manufacturing of lightweight components through exceptional degrees of freedom of design and superior utilisation of materials, in comparison to subtractive manufacturing techniques [3]. In general, AM processes for metallic materials can be broadly categorised into powder-bed, powder-feed and wire-feed systems in combination with an energy source such as electron beam, laser or electric arc [4]. One of the key differences between these processes is the corresponding building volume and the related energy input required for melting the consumable [4]. For powder-bed processes, the build volumes are rather small but with the advantageous ability to produce high resolution parts and internal features under controlled compliance with the dimensions. For powder-feed processes in comparison to powder-bed, the build volumes are averagely larger, enabling volumetric scale-up of part sizes [5]. In contrast to powder-based methods, wire-feed metal deposition (WFMD) provides unique advantages such as exceptional deposition rates, more efficient usage of material and superior capabilities to produce large part sizes, as the process does not require a space-restricting gas or vacuum chamber [4,6,7]. The greater availability and most often lower costs for consumable alloys as wire material in comparison to powder material, is also highly beneficial [2]. The utilisation of a laser beam as heat source instead of an electric arc offers the advantage to control the heat input, i. e. the energy input per mass of material, more precisely and by using a laser beam instead of an electron beam, no vacuum is required.

Simultaneously, to achieve weight savings, materials with high strength-to-density ratio such as aluminium alloys are utilised in structural components [8]. Nowadays, properties such as formability, corrosion resistance, recyclability, good thermal and electrical

---

conductivity have led to aluminium being one of the most used light-weight materials in aviation, automotive and marine industries [1, 9]. In this investigation, a 5xxx series aluminium alloy is chosen because it offers a very high mechanical strength among the non-heat-treatable aluminium alloys, suitable corrosion resistance and good weldability characteristics [10].

During the LMD process, a single bead layer is deposited onto a substrate, which is in this study also a 5xxx series aluminium alloy. The initial layer is followed by subsequent layers added on top or aside to ultimately constitute a three-dimensional structure. It is well known that processing parameters and conditions, such as inter-layer waiting time and pre-heating, strongly affect the process stability as well as resulting material characteristics and part properties [11]. For complete melting of the consumable wire, the required laser power of wire-based LMD is significantly higher in comparison to powder-based methods since it amounts up to several kilowatts instead of only a few hundred watts, respectively [4]. The wire material is exposed to a complex thermal load cycle: due to rapid solidification and partial re-melting, phenomena such as directional heat fluxes as well as substantial local and global thermal gradients can be observed within the structure. The accompanied inhomogeneous thermal expansions during heating and cooling phases of the process lead to strains, stresses and distortions in the deposited beads and surrounding areas. Particularly, heat accumulation as well as temperatures near and above the solidus temperature in adjacent material can promote geometrical instabilities during the formation of each deposited bead; affecting the structural properties such as wall thickness and geometric integrity. Furthermore, undesired buckling in the deposited layers and the substrate plate as well as early failure of the structure during its application might be provoked, when no appropriate process control is applied.

On the microscale, varying temperature gradients and solidification rates during WFMD can cause highly diverse grain size distributions within the microstructure that lead to locally inhomogeneous properties. The formation of these local microstructural variations is strongly affected by the employed process parameters. For wire-based LMD of Al-Mg, the use of low laser beam irradiances leads to the formation of an alternating microstructure with fine equiaxed grain zones and columnar grain zones [12]. A similar effect was observed in WAAM of Al-Mg for low heat inputs by using polarity variation [13] or online vortex cooling [14]. Also along the building direction, the grain size can change from layer to layer due to changing temperature gradients [15]. The temperature distribution within the melt pool and the melt pool dimensions have an influence on the loss of alloying elements, e.g. of Mg, during WAAM of Al-Mg [16]. Thus, the local distribution of alloying elements such as Mg within the bead as well as the local properties could become inhomogeneous. In addition, the solidification cracking of Al-Mg can be increased by the change of the chemical composition, microstructure and temperature gradient [17]. In this regard, melt pool temperatures above evaporation temperature and low cooling rates promote the formation of overheating porosity [14]. Heat input regimes have been developed for controlling the porosity formation during WAAM of Al-Mg [18,19]. These issues present key challenges for WFDM in general but are also of great relevance for wire-based LMD. To establish a reproducible and stable LMD process for producing macroscopic defect-free parts, it is essential to first identify and predict the highly inhomogeneous temperature distribution and adapt process parameters [20]. To expand understanding beyond the information contained in experimental measurements, numerical process simulations are very useful [4], if not even necessary.

Based on the first finite element (FE) modelling approaches of welding processes developed in the 1970s and the close similarity of fusion welding such as laser beam welding (LBW) to LMD, adopting these approaches effectively enabled simulation of AM processes [21–23]. Most commonly, transient temperature models are used with a travelling heat source, combined with either a quiet or inactive element approach, to account for the newly added material [24]. Such a

simulation approach was used in [20,25–27], for example, to predict the resulting temperature distribution during the LMD process.

Up to now, the number of combined experimental and modelling studies with respect to wire-based LMD of aluminium alloys is scarse [26,27]. Investigations were focused on either powder-based LMD [28–35] or wire-arc additive manufacturing (WAAM) [26,36–39], typically using materials such as steel [27,37,40], titanium [41,42] and aluminium alloys [43]. Investigations also involved computational fluid dynamics (CFD) simulations of the melt pool and the molten metal during liquid bridge transfer during WAAM [44–46]. Regarding wire-based LMD, the processing of titanium alloys was predominantly investigated, so far [24,41,47]. However, to the knowledge of the authors, a combined experimental-numerical study on Al-Mg parts produced by LMD with focus on temperature distributions, residual stresses and distortions is not available, yet.

The objective of this work is to set-up, calibrate and employ a numerical thermal-model on the basis of experimental observations for predicting the evolution of the temperature distribution. Furthermore, the thermal model is sequentially coupled to a mechanical analysis for predicting and minimising residual stresses and distortions within the final structure via adjustments of process parameters and conditions. The computed temperature distributions are validated through comparison to experimental results. Experimental measurements of temperatures during LMD and identification of resulting geometrical features have been performed, on the one hand, to define input details for the model, such as melt pool depth, and on the other hand, to validate the thermal model. Temperatures occurring during LMD were quantified through thermocouple and thermography measurements. The melt pool and the cross-sectional area of deposited material were determined based on macrographic images of the specimens and high-speed camera sequences. Influential process parameters, such as the inter-layer waiting time (ILWT) and deposition strategy, as well as conditions, such as pre-heating of the substrate and heating of the process surrounding air, on final-part residual stresses and distortions, are investigated.

This study is structured as follows: first, the methodology of experiments including the process, materials and measurement techniques are explained. Then, theoretical background on the thermo-mechanical analysis is provided, followed by a description of the model calibration, as well as the process simulation and comparison to the experimental results. Ultimately, a numerical process optimisation was performed, where process parameters and conditions are adjusted with respect to reducing residual stresses and distortions of the final structure.

2. Methods and materials

2.1. Laser metal deposition process

As heat source for the LMD process, an ytterbium fibre laser YLS-8000-S2-Y12 (IPG Photonics Corporation) with a maximum laser power of 8 kW (continuous wave) was utilised. The laser was attached to an YW52 Precitec optical head, which was mounted onto the z-axis (building direction) of a CNC-supported machining centre (IXION Corporation PLC). Alongside the optical head, the wire-feeding system (with a fixed feeding angle of 35° in relation to the substrate surface plane) and the nozzle for local shielding with argon gas, to prevent reactions between molten material and atmospheric elements, were installed. In Fig. 1(a), the LMD process for generating a wall-like structure consisting of several single bead layers is illustrated.

The wire material was fed unidirectional in dragging manner, melted by a defocused laser beam and deposited onto the substrate, as illustrated in Fig. 1(a). Once the deposition of one layer with a length of 100 mm was completed with the process parameters listed in Table 1, a mandatory height offset in building direction, which can slightly vary, and the return to the starting point of the deposition path was accounted
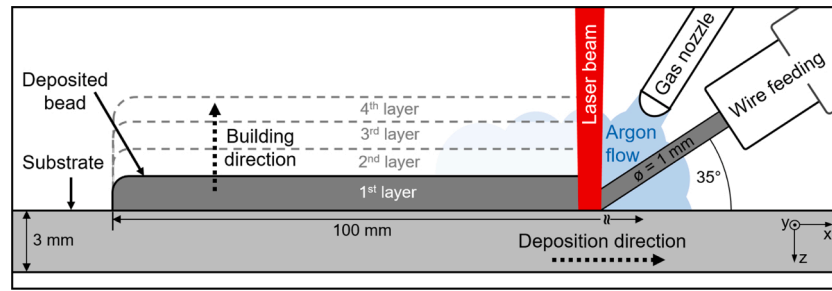
(a)
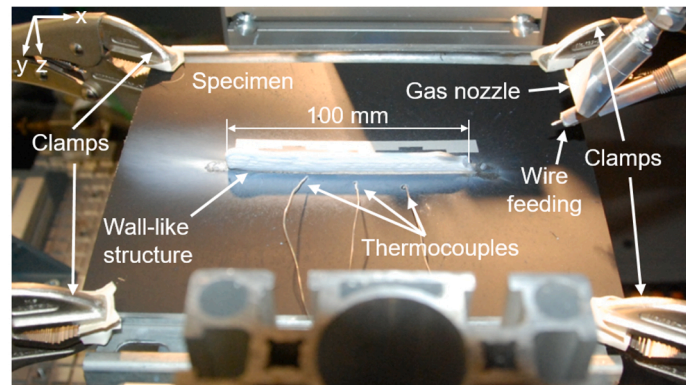
(b)

Fig. 1. (a) Schematic of LMD process, where the unidirectional deposition of several single bead layers is performed to build a wall-like structure with a laser spot diameter of 1.6 mm; a laser power of 4000 W, a wire-feeding rate of 10 m/min with a 35° angle in relation to the plane of the moving substrate plate; (b) side view of clamped substrate with a deposited wall-like structure, fixed positions of thermocouples, shielding gas nozzle and wire feeding in their final position after LMD.

Table 1
LMD process parameters employed in the experiments.

Parameter	Value
Laser power	4000 W
Wavelength	1.070 μm
Fibre diameter	300 μm
Focal length	300 mm
Collimator length	150 mm
Rayleigh length	24.55 mm
Spot diameter (in focus)	746 μm
Defocussing	−23 mm
Spot diameter (on substrate)	1.6 mm
Deposition velocity	1 m/min
Wire feeding rate	10 m/min
Shielding gas flow rate	10 l/min
Vertical offset for layer 2	2.4 mm
Vertical offset for layers 3 and 4	1.7 mm
Initial substrate temperature	≈20 °C

for during the re-positioning of the optical head for depositing the subsequent layer in uniaxial direction. To provide enough time for the re-positioning, an inter-layer waiting time of 60 s was selected. To avoid unintended reflections of the laser beam into the laser optics during the deposition of the first layer, the surface of the substrate was sandblasted. For the subsequent layers, it is assumed that properties such as the convex shape of the previously deposited bead layer prohibited unintended reflections of the laser beam sufficiently. The specimen is clamped at a fixed position as shown in Fig. 1(b). The AA5087 wire was 1 mm in diameter and the AA5754 substrate plate featured 200 mm × 150 mm × 3 mm in length, width and thickness, respectively, see Fig. 2 (a). By using the constant LMD process parameters listed in Table 1, an effective melting of wire material is assured as a production of

homogeneously deposited structures with only small pore occurrences between the layers but without macroscopic defects was achieved [48].

2.2. Temperature measurements

Point-wise thermal histories were obtained via thermocouples of type-K with a diameter of 0.5 mm. Conductive paste (*Keratherm*, *KP*68) was applied between the thermocouples and the specimen in order to assure the highest possible conduction. Measurement positions (T1, T2 and T3) were chosen to be as close to the heat source as possible but with enough distance to avoid damage of the thermocouples, as shown in Fig. 2(a). The thermocouples were positioned in drilled holes (diameter = 0.55 mm, depth = 0.75 mm) on the top surface with distances of 4 mm, 6 mm and 8 mm to the deposition path along its length and 20 mm apart from each other. It should be noted that maximum temperatures, especially in the melt pool, are significantly higher than the ones measured but could not be determined due to the limited heat resistance of the thermocouples. However, as the distance of the thermocouples to the deposition path is increased incrementally, the spatial and temporal mapping of the temperature field, i.e. at different positions at different times in the substrate, becomes possible. This serves as valuable input information for the set-up of the model.

Thermography measurements of the temperature field, across the entire bottom surface area of the specimen, were acquired through the utilisation of the IR-camera *PI 400* from *Optris*, for a temperature range from −20 °C to 900 °C. The system was positioned at a distance of 170 mm and pointed to direction of the bottom surface in perpendicular direction to the specimen surface plane, see Fig. 2(b). For ensuring high sensitivity of the thermography measurements, the emission of the substrate surfaces was increased by coating them with temperature resistant matt black paint. The thermography was calibrated by correlating temperature measurements of three additional thermocouples on
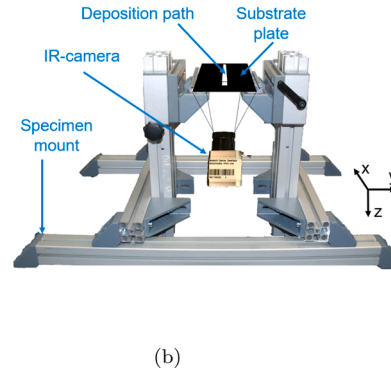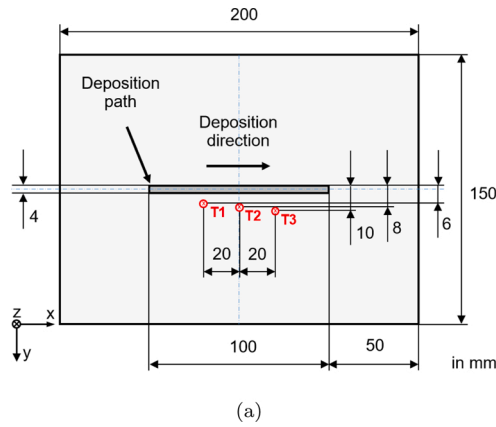
Fig. 2. (a) Top view on specimen surface with positions of the three thermocouples (T1, T2, T3) equidistant to one another but with increasing distance to the deposition path. All dimensions in mm. (b) The specimen mount and the IR-camera positions with a distance of 170 mm and an angle of 10° to the substrate plate.

the bottom surface through adjustment of the emissivity. This led to a good agreement continuously throughout the process for a temperature regime from 20 °C to 500 °C.

2.3. Characterisation methods

For the identification of the melt pool length during LMD of several layers, a high-speed camera *CR-S3500-M* (*Optronis GmbH*) with a *Nikon AF Micro Nikkor* 60 mm prime lens was mounted onto the *z*-axis to record the solidification of the melt pool. The distance of camera to the *x-z*-plane of the deposited wall-like structure measured 160 mm with an angle of 10° in relation to the *x-y*-plane of the substrate. The recording frequency was adjusted to 2000 frames per second with an exposure time of 250 μs to capture the deposition. A *Cavilux* laser unit with a wavelength of 690 nm from *Cavitar Ltd.* was used for sufficiently lighting the image frame, complemented by a narrow-band-pass filter.

For the determination of layer heights, two measurement techniques were applied. During the process, a digital calliper gauge was placed at the beginning of the previously deposited layer to account for the layer-offset to the substrate in building direction and to assure proper deposition of the next layer. After the process, specimens were cut out at the centre of the wall, embedded in polymer, grinded and polished with an oxide polishing suspension compound. An inverted optical microscope *Leica DMI 5000M* with polarised light support was used to obtain cross-sectional macrographs and precisely determine layer widths and recorded heights of the wall-like structure.

2.4. Materials

Two Al-Mg alloys were deployed in the LMD experiments: AA5087 (AlMg4.5MnZr) as wire and AA5754 (AlMg3) as substrate material. The solidus-liquidus temperature ranges of these two alloys are 610-640 °C for AA5087 [49] and 574-638 °C for AA5754 [50]. Using these two 5xxx series aluminium alloys led to good layer-substrate bonding since both show a comparable thermal behaviour. Nevertheless, identification of the penetration depth of the first layer into the substrate is easily possible due to the differing microstructures of melted and unmelted material.

Thermophysical material properties such as thermal conductivity k and specific heat capacity c_p strongly affect the transient temperature field distribution. In conjunction with Young's modulus E and yield stress σ_y, these properties influence residual stresses and distortion. Thus, these material properties have to be considered temperature dependent for the numerical analyses [51–54]. The initial thermophysical properties of the wire and substrate materials at room temperature, provided by the supplier [49,50], were extrapolated to the higher temperature regime according to slopes provided by Mills et al.

[55] and Zhu et al. [51] for related aluminium alloys. Thermal softening was considered through a temperature dependent yield stress [23,56]. Particularly for Al-Mg alloys, according to Zhu et al. [51], the dependence of the yield stress σ_y on the temperature T can be approximated by using the following formula:

$$\sigma_y = \begin{cases} 0.05\sigma_{y0} + \dfrac{400 - T}{300} \cdot 0.95\sigma_{y0}, & 100 < T < 400°C \\ 0.05\sigma_{y0} \approx 10\,\text{MPa}, & T \geq 400°C \end{cases} \tag{1}$$

with σ_{y0} as the yield stress at room temperature. A cut-off temperature of 400 °C, which is approximately 2/3 of the solidus temperature of the material, is employed to keep the Young's modulus and yield stress beyond that temperature constant and above a value of zero, to avoid numerical instabilities and still be computational efficient [51,57,58]. The employed temperature dependent thermal and mechanical properties for both materials are shown in Fig. 3. The density and thermal expansion coefficient are assumed to be identical for both alloys and temperature-independent with $\rho = 2.66\,g/cm^3$ [49,50] and $\alpha = 2.4 \cdot 10^{-5} K^{-1}$ [59], respectively. This is in agreement with the study by Zhu et al. [51], who showed for welding simulations of AA5052-H32 that there is negligible influence of temperature-dependent ρ and α on the temperature field as well as on residual stresses and deformation, respectively.

3. Numerical LMD process model

The employed temperature model is based on a simplified model setup for a transient heat transfer analysis of Al-Mg during LMD [25], where the heat transfer during the LMD process is considered to be solid; thus, phase transformation phenomena above the liquidus temperature are neglected and the temperature evolution above is not further investigated. For the mechanical analysis, isotropic material behaviour is assumed. Despite the significant influence of the fluid flow on the shape of the local melt pool [60], this aspect was ignored in this study because the influence on the global temperature distribution and deformations is assumed to be negligible [61]. Further, it is presumed, that the mechanical properties and behaviour do not influence the temperature evolution [62].

3.1. Transient heat transfer model

The temperature field during LMD can be analysed through solving the transient nonlinear heat transfer equation. The three-dimensional heat equation in Cartesian coordinates x is defined by the partial differential equation:
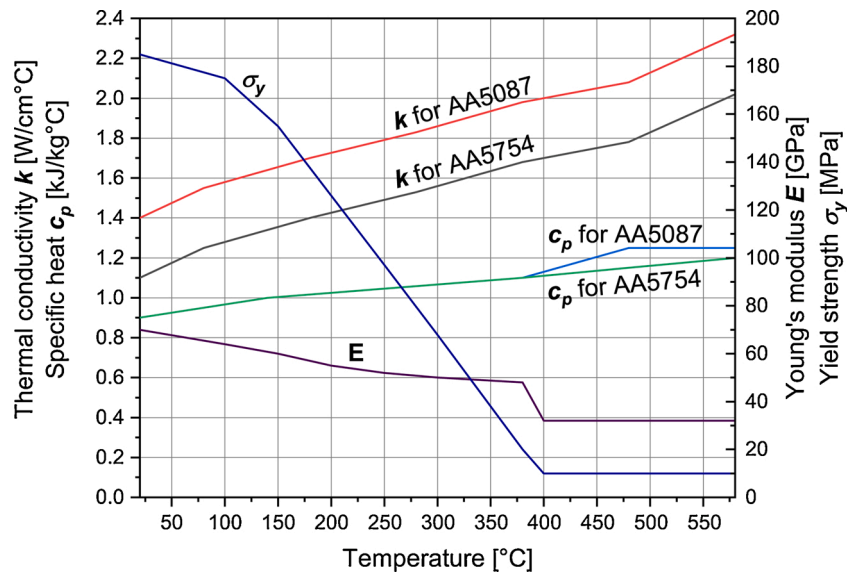
Fig. 3. Temperature dependent mechanical material properties: Young's modulus E in GPa and yield strength σ_y in MPa are considered to be identical for both AA5087 and AA5754; temperature dependent thermal material properties: thermal conductivity k in W/cm°C and specific heat capacity c_p in J/g°C for AA5087 and AA5754, respectively [49–51,55].

$$\rho c_p(T)\frac{\partial T(\mathbf{x},t)}{\partial t} = -\nabla \cdot \mathbf{q}(\mathbf{x},t) + Q_{HS}(\mathbf{x},t) \qquad (2)$$

with mass density ρ, specific heat capacity $c_p(T)$, transient temperature $T(\mathbf{x},t)$, time t and the energy introduced by volumetric source term $Q_{HS}(\mathbf{x},t)$. As the heat flux linearly depends on the temperature gradient, the heat flux vector is determined by:

$$\mathbf{q} = -k(T)\cdot\nabla T(\mathbf{x},t) \qquad (3)$$

with thermal conductivity $k(T)$. In addition, surface convection and radiation of the specimen are considered through the boundary conditions as described by the following equation:

$$q_{surface}(\mathbf{x},t) = h[T - T_0] + \varepsilon \cdot k_B[T^4 - T_0^4] \qquad (4)$$

where h is the convection coefficient, T_0 the ambient room temperature, ε the emission coefficient and k_B the Boltzmann constant.

The moving heat source consists of a three-dimensional energy distribution, in accordance to the work of Goldak et al. [63], which was imposed onto the re-activated elements representing the deposited material. For the LMD process simulation, a bounded heat source with a normal-distribution shape is used according to the approach by Karkhin et al. [64] and Herrnring et al [65]. Specifically, the energy is bounded to a local cuboid domain defined as: $[\xi', \xi''] \times [\eta', \eta''] \times [\zeta', \zeta'']$, illustrated in Fig. 4. The total energy distribution can then be described as:

$$Q_{HS}(\xi,\eta,\zeta) = f_\xi(\xi)\cdot f_\eta(\eta)\cdot f_\zeta(\zeta)\cdot Q_{laser} \qquad (5)$$

where Q_{laser} represents the effective laser power and f_ξ, f_η, f_ζ the Gaussian energy distribution functions along the ξ-, η-, and ζ-axes of the local coordinate system of the cuboid domain, as shown in Fig. 4. The Gaussian distribution in one of the three local directions, for example in ξ-direction, is defined by:

$$f_\xi(\xi) = \frac{2}{\sqrt{\pi}}\left[\xi_e\left[\mathrm{erf}\left(\frac{\xi''}{\xi_e}\right) - \mathrm{erf}\left(\frac{\xi'}{\xi_e}\right)\right]\right]^{-1} e^{-\left[\frac{\xi}{\xi_e}\right]^2} \qquad (6)$$

with ξ' and ξ'' as the local boundaries of the heat source and $\mathrm{erf}(\bullet)$ as the Gauss error function. ξ_e is the geometrical energy distribution parameter, representing the distance between the heat source origin, where the energy has its maximum value, to the point where the energy has

declined to $1/e$ of this maximum value.

To confirm sufficient energy transmission between the heat source volume and the model mesh, a mesh-convergence study has been performed. The complete set of geometric heat source parameters is listed in Table 2, which led to a heat source similar to the experimental findings discussed in the later Section 3.3.3.

3.2. Mechanical coupling

Sequential mechanical coupling of the heat transfer analysis was achieved by loading the thermal history as a predefined temperature field into the mechanical analysis. Since significant cooling rates occur during LMD for welding and additive manufacturing, modelling approaches that were originally established for casting processes can also be applied here, where the constitutive material model of the LMD process is consequently classified as a casting process. The utilised simulation environment is ABAQUS and the material model is implemented as a user-subroutine. Since the standard von-Mises model executed in ABAQUS, suffered severe convergence problems during the reactivation of elements, these could be overcome by the modified material model proposed by Chiumenti et al. [66]. For the stabilisation of incompressible material behaviour in the liquid state, a mixed u/p-FE formulation[1] was used in the mechanical analysis. In this approach, the evolution of plastic strains ε^p is determined through the application of an associative flow rule in conjunction with a von-Mises flow criterion. In the material model, aggregate state above the liquidus temperature is not considered. Thus, the material behaviour in the mushy zone, between solid and liquid aggregate state, can be described by the solid fraction f^s, based on the work of Chiumenti et al. [66]. A small strain theory is used for simplicity because only small deformations are assumed after solidification in the LMD process. Thus, the total strain ε consists additively of the elastic strain ε^e, plastic strain ε^p and thermal strain ε^Θ as:

$$\boldsymbol{\varepsilon} = \boldsymbol{\varepsilon}^e + \boldsymbol{\varepsilon}^\Theta + \boldsymbol{\varepsilon}^p. \qquad (7)$$

Subsidiary, the plastic strain evolution is defined through

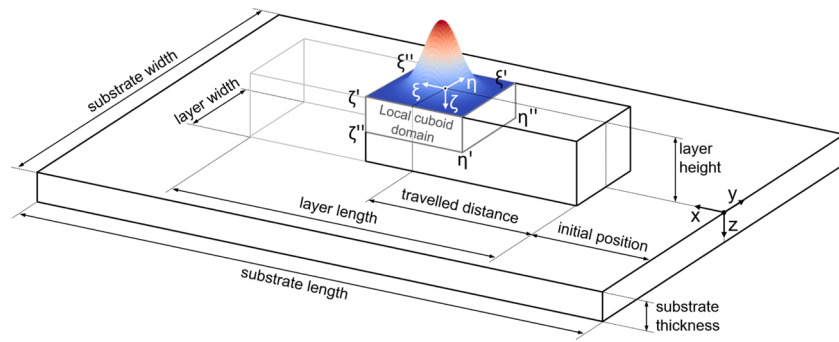[1] u and p referring to displacement and pressure, respectively.

Fig. 4. Illustration of the local cuboid domain $[\xi, \eta, \zeta]$ of the travelling heat source distribution in relation to the fixed global coordinate system $[x, y, z]$ of the substrate plate and deposited layers.

Table 2
Geometric energy distribution parameters of the applied heat source in reference to its local cuboid coordinate system, where directions between ξ', ξ'' correspond to the global x-axis, η', η'' correspond to the global y-axis, ζ', ζ'' correspond to the global z-axis and ξ_e, η_e, ζ_e represent shape-function parameters in these particular directions.

ξ'	ξ''	η'	η''	ζ'	ζ''	ξ_e	η_e	ζ_e
− 4.0 mm	2.0 mm	− 2.500001 mm	2.500001 mm	0.0 mm	1.5 mm	100 mm	100 mm	100 mm

$$\dot{\boldsymbol{\varepsilon}}^p = \dot{\gamma}\sqrt{\frac{3}{2}}\frac{s}{||s||} \tag{8}$$

where $\dot{\gamma}$ is the plastic multiplier and s the stress deviator. The plastic multiplier is described by a modified Bingham-model[2] :

$$\dot{\gamma} = \frac{1}{\eta}\left\langle\sqrt{\frac{3}{2}s:s} - \sigma_y f^s(T)\right\rangle \quad f^s(T) \in [0,1] \tag{9}$$

where viscoplastic behaviour is introduced by the viscosity parameter η, which is assumed to be $\eta = 20\,\text{kg}/(\text{m s})$. The temperature dependent solute fraction $f^s(T)$ is used to scale the yield stress σ_y accordingly: for purely solid material, thermo-elastic-viscoplastic behaviour is implemented in the material model through $f^s = 1$; whereas for fully liquid material, pure viscous behaviour is introduced via the solid fraction $f^s = 0$. With a modified Hooke's law, the thermal and elastic strains are turned silent in the mushy zone by

$$\boldsymbol{\sigma} = \frac{K}{f^s}\varepsilon_v^e \mathbf{I} + 2\frac{G}{f^s}\text{dev}(\boldsymbol{\varepsilon}^e) \tag{10}$$

with **I** being the second order identity tensor, ε_v^e the volumetric elastic strain, K the bulk modulus and G the shear modulus. Considering the plastic multiplier from Eq. (9) in Equation (8) leads to:

$$\dot{\boldsymbol{\varepsilon}}^p = \dot{\gamma}\sqrt{\frac{3}{2}}\frac{s}{||s||} = \frac{3}{2}\frac{1}{\eta}\mathbf{s}, \\ \boldsymbol{\varepsilon}^e = 0, \quad \varepsilon_v = \text{const.}, \quad \text{if} \quad f^s = 0. \tag{11}$$

For the definition of the solid fraction f^s, solidification is assumed to occur without diffusion in the solid phase. Thus, the evolution equation of f^s between the liquidus temperature T_L and the solidus temperature T_S can be defined as [66]:

$$f_s(T) = 1 - \left[\frac{T_F - T}{T_F - T_L}\right]^{\frac{1}{\kappa-1}} \quad \text{with} \quad \kappa = \frac{T_F - T_L}{T_F - T_S} \tag{12}$$

with T_F as the fusion temperature and the partition coefficient κ as the ratio between solid and liquid composition at equilibrium. Since the equilibrium composition between solid and liquid phases can be

considered constant throughout the solidification, an instantaneous solidification of the pure component is assumed at solidus temperature; thus, linear regularisation via a temperature ΔT is applied for simplicity [66]:

$$f_s(T) = \begin{cases} 1 - \left[\frac{T_F - T}{T_F - T_L}\right]^{\frac{1}{\kappa-1}} & \text{for} \quad T_S + \Delta T \leq T \leq T_L \\ [1 - f^s(T_S + \Delta T)]\left[\frac{T_S - T}{\Delta T}\right] + 1 & \text{for} \quad T_S \leq T \leq T_S + \Delta T \end{cases} \tag{13}$$

with $T_F = 660°C$ and $\Delta T = 20°C$. Herrnring et al. [65] outlined the implemented algorithm, where isotropic material hardening is considered.

3.3. Model set-up

3.3.1. Model and mesh

The model of a 4-layered structure created for this study is depicted in Fig. 5. The element size was chosen to be most fine in the region of the deposition path and its surrounding area. In particular, the elements constituting the deposited layers as well as the elements in close vicinity of the deposition path have dimensions of 0.5 mm in each spatial direction. With increasing distance to the deposition path, the element size is coarsened towards the edges of the specimen. Based on a convergence study, this mesh size can be estimated as sufficient, which is in agreement with other investigation, such as Costa et al. [67], Tran et al. [47] and Ding et al. [56].

3.3.2. Material deposition

Two main element approaches for modelling the deposition of material for an FEM process simulation are reported in literature: the inactive element approach and the quiet element approach [24,57,68]. Inactive elements are not considered in the analysis until re-activation; thus, only the nodal degrees of freedom of active elements are taken into account during the analysis. Step-wise re-activation leads to the incorporation of additional elements and to an increase in degrees of freedom of the model. Quiet elements are permanently contained in the model but are initially assigned material properties that have no effect on the analysis, such as a closely-to-zero reduced Young's modulus or thermal conductivity. These quiet elements are then re-assigned properties that

---

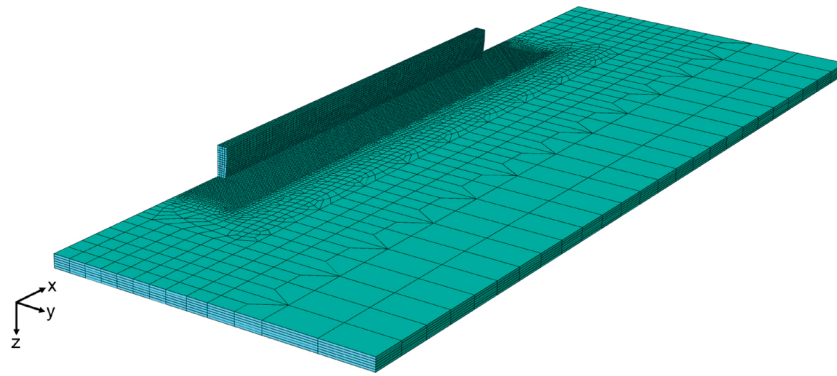[2] Note that the Macaulay brackets $\langle\bullet\rangle$ are used.

Fig. 5. Symmetric FE-model of the LMD substrate with a 4-layered wall-like structure including mesh discretisation.

represent the realistic material values and affect the analysis. For the heat transfer analysis, three-dimensional heat transfer elements (DC3D8) were used and the inactive element approach was implemented. The successional re-activation of elements was realised via a Python script. For the mechanical analysis, a combination of both quiet and inactive elements was implemented during the mechanical coupling to reach convergence of the analysis and to optimise computational time, as reported by Michaleris [24]. The inactive elements were switched on in a layer-wise manner as quiet elements (C3D8H) with a reduced Young's modulus of 10 MPa. They were then assigned realistic properties triggered by the simultaneous occurrence of a negative temperature gradient and the solidus temperature. The quiet element approach was implemented with the material model outlined in the previous section. An exemplary computational time comparison of using either a solely quiet element approach or a combined inactive-quiet element approach, demonstrated a time reduction of ≈ 38% for the combined inactive-quiet element approach.[3]

Surface convection and radiation are imposed as thermal boundary conditions onto the outer surfaces of the substrate and bead-wall geometries as well as onto the inter-layer surfaces on top of the active elements of the currently deposited layer. The convection coefficient was set to 30 W/(m^2 K), representing cooling at air [51] and the unit-less emission coefficient to 0.3 [69]. The initial temperature of the substrate plate was set to room temperature of 20 °C. The mechanical boundary conditions were the imposed symmetry in *x-z*-plane as well as the fixed boundaries at the long edge on the bottom and at the corners on the top of the substrate plate, according to the experimental clamping conditions in Fig. 1(b).

3.3.3. Layer-wise increase of cross-sectional area and melt pool depth

The height and width of added material and the related depth of the melt pool is taken from cross-sectional macrographs of deposited wall-like structures consisting of incrementally rising number of layers, as shown in Fig. 6. The height of the layers is related to a number of re-activated elements making up the added layers, which measure 2.5 mm for the first layer and 1.5 mm for the consecutive layers. The number of re-activated elements contained in one element-set corresponds to the amount of added material. Based on the macrographs, the melt pool depth is assumed to measure approximately 2.5 mm, which was used to adjust the numerical heat source parameters in Table 2. Horizontal nodal positions were adjusted to experimental width-observations. The total bead width measured 4 mm at the first layer, rising linearly to 5 mm at the third layer and remained constant there-after up to the fourth layer. Curved surface were not taken into account since effects such as surface tension are neglected, as commonly done for

process simulation of AM in literature [42].

4. Process simulation

4.1. Temperature prediction and comparison to experimental results

The numerical transient heat transfer analysis was assessed by extracting the temperatures over time at three nodal points T1, T2 and T3 in the FE-model, as shown in Fig. 7, corresponding to the experimental positions of the thermocouples on the top surface of the substrate, see Fig. 2.

The comparisons between numerical and experimental results show good agreement regarding temperature maxima T_{max} and cooling behaviour at all three positions, see Fig. 8(a–c), as well as with respect to thermal gradient evolutions between the positions T1 and T2, T2 and T3, as well as T1 and T3, see Fig. 8(d–f). These one-dimensional thermal gradients $T_{\text{grad},T_i,T_j} = -\frac{\partial T}{\partial s} = -\frac{T_j - T_i}{s}$ were determined by the temperature difference between two measurement positions $T_j - T_i$ with respect to the interjacent distance *s*. Experimental results consist of averaged values based on five separate measurements and are complemented by the corresponding standard deviations which are marginal and indicate a good experimental reproducibility of the process. Temperature maxima and minima at the three positions show different magnitudes during the deposition of four layers. The highest temperature maxima occur at position T1, as it is closest to the deposition path; whereas, the temperature maxima are gradually less significant at position T2 and T3, respectively, as the distance to the deposition path is incrementally increased. An important notice is that the maximum temperatures near and in the melt pool are substantially higher than the ones measured but a further decrease in distance to the melt pool would have led to damaged thermocouples and is therefore not accessible.

The drop of temperature during cooling, after the deposition of each layer from $T_{max,n}$ to $T_{min,n+1}$, is reduced with rising layer numbers, as the temperature maximum is incrementally reduced and the minimum gradually increased (see Fig. 8 (a)-(c)). Two conditions contribute to this behaviour: gradual heat-up of the specimen and increased distance between melt pool and thermocouples on the substrate because of added height by the growing number of layers [70]. After the deposition of one layer, the waiting time before the deposition of the next layer is not sufficient to allow cooling down of the specimen completely back to initial room temperature. As opposed to layer-wise falling of temperature maxima at T1 and T2 during the deposition of the four layers, there is a minimal increase in the temperature maxima at T3 from first to second and third layer. Due to the larger distance to the travelling heat source, maxima are lower at T3 compared to T1 and T2 but owed to the gradual heat-up of the specimen, thermal conductivity is increased, causing growing temperature maxima up until the deposition of the third layer. The most significant thermal gradient within the specimen occurs during the deposition of the first layer due to the most significant

---

[3] Used were 4 Intel Xeon CPU's with 2.1 GHz each and 8 × 32 GB DIMM synchronous RAM units with 2666 MHz.
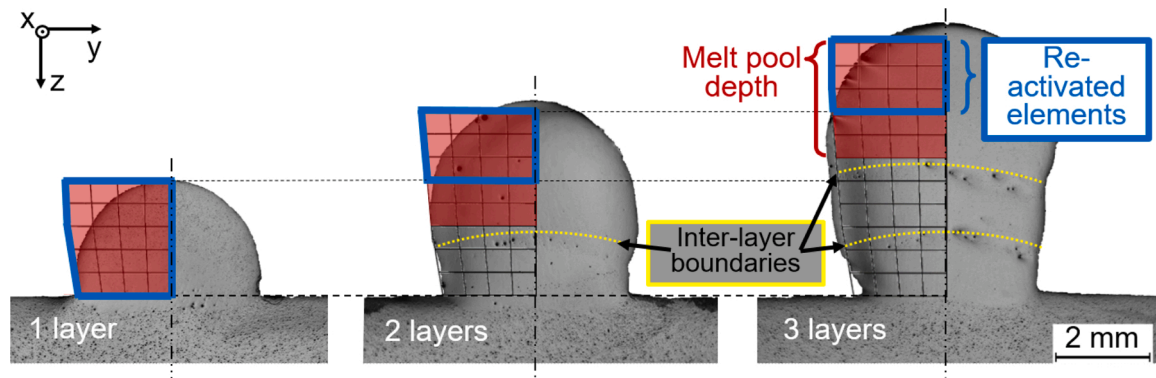
Fig. 6. Macrographs of increasing number of deposited layers with inter-layer boundaries indicated by small pores in correspondence with superimposed mesh discretisation, including cross-sectional areas of activated element-sets and melt pool depth. Due to symmetry of the problem, only half of the model is simulated.
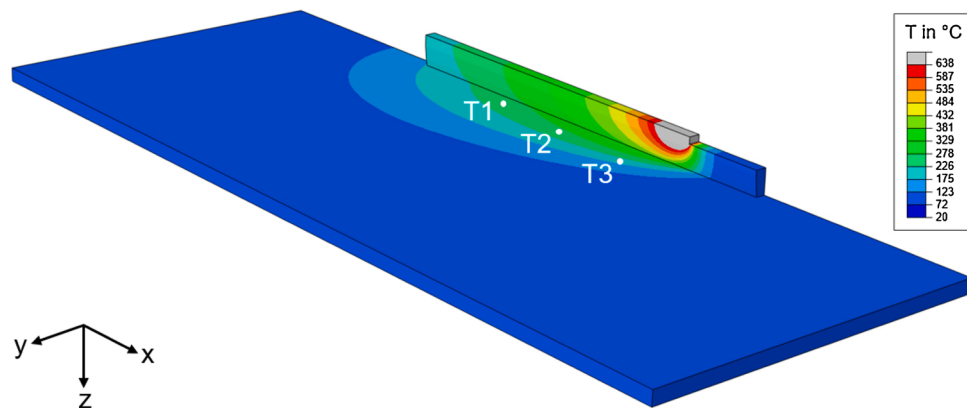

Fig. 7. Simulated temperature distribution during LMD including nodal positions for extraction of temperature curves equivalent to thermocouple positions T1, T2 and T3, see Fig. 2.

temperature difference between the solidus temperature of the deposited material and the substrate at initial room temperature. Since the complete structure is heated up layer-wise, this temperature difference decreases, leading to lower thermal gradients, see Fig. 8(d)–(f). The extrema of the thermal gradients between the different measurements positions (T1 and T2, T2 and T3 as well as T1 and T3) are decreasing in magnitude with rising distance to the deposition path. The larger the space between the positions and the deposition path, the less different the highest and lowest thermal gradient values with growing layer number.

Additionally, the previously deposited layers are relatively narrow, enabling only reduced thermal conduction within the wall-like structure. This leads to an elongation of the melt pool. The more material volume surrounds the melt pool, the higher is the possible thermal conduction through that material, which is affirmed by the increasing length of the melt pool with rising number of layers [71], as shown in the high-speed images of the LMD process, recorded during the deposition of three layers in Fig. 9(a)–(c). The length of the melt pool is increasing from 9 mm during the deposition of the first layer, over 12 mm during the second layer to 15 mm during the third layer.

For obtaining further information on the heat accumulation, the cooling behaviour across the area of the bottom surface of the substrate was recorded with an infrared camera. The time period of cooling was analysed immediately after the end of the deposition of the first layer. The temperature peak value is declining during cooling and shifting its position from the end of the deposition path, where the laser last interacted with the material, towards the centre of the specimen. This indicates a moving location of heat accumulation, see Fig. 10(a)–(d), which can be correlated to areas of significant residual stress and

displacement, as reported in the following section.

4.2. Prediction of residual stresses and deformations

There is a strong relation between the observed inhomogeneous heat distribution with significant temperature gradients within the structure during LMD and the qualitative occurrence of computed residual stresses and distortion after LMD and substrate unclamping, as can be seen in Fig. 11.

In general, residual stresses are a result of the inhomogeneous heat-up and cool-down of the specimen during the deposition process [72]. The thermal strains lead to local volumetric material enlargement with increasing temperatures. This produces a deformation of the material. For deposited material changing from liquid to solid state, internal stresses arise during solidification and further cooling due to shrinkage associated with decreasing temperatures since the surrounding base material hinders the contraction of the deposited layer. The predominant longitudinal stresses in the deposit create major transversal stresses in the base material to fulfill the overall equilibrium conditions [73]. In combination with substrate clamping during LMD, this can lead to the generation of residual stresses and undesired deformations within the complete specimen [62,74].

The residual stresses in the upper part of the deposited wall-like structure caused by shrinkage according to inhomogeneous heat distribution lead to deformation of the structure, as can be seen from the stresses depicted in Fig. 11(a). The simulated σ_{xx} residual stresses are determined to be close to the yield strength of $\sigma_y = 185$ MPa. Stress concentrations occur within and along the deposited wall-like structure as well as at the beginning and at the end of the deposition path. The
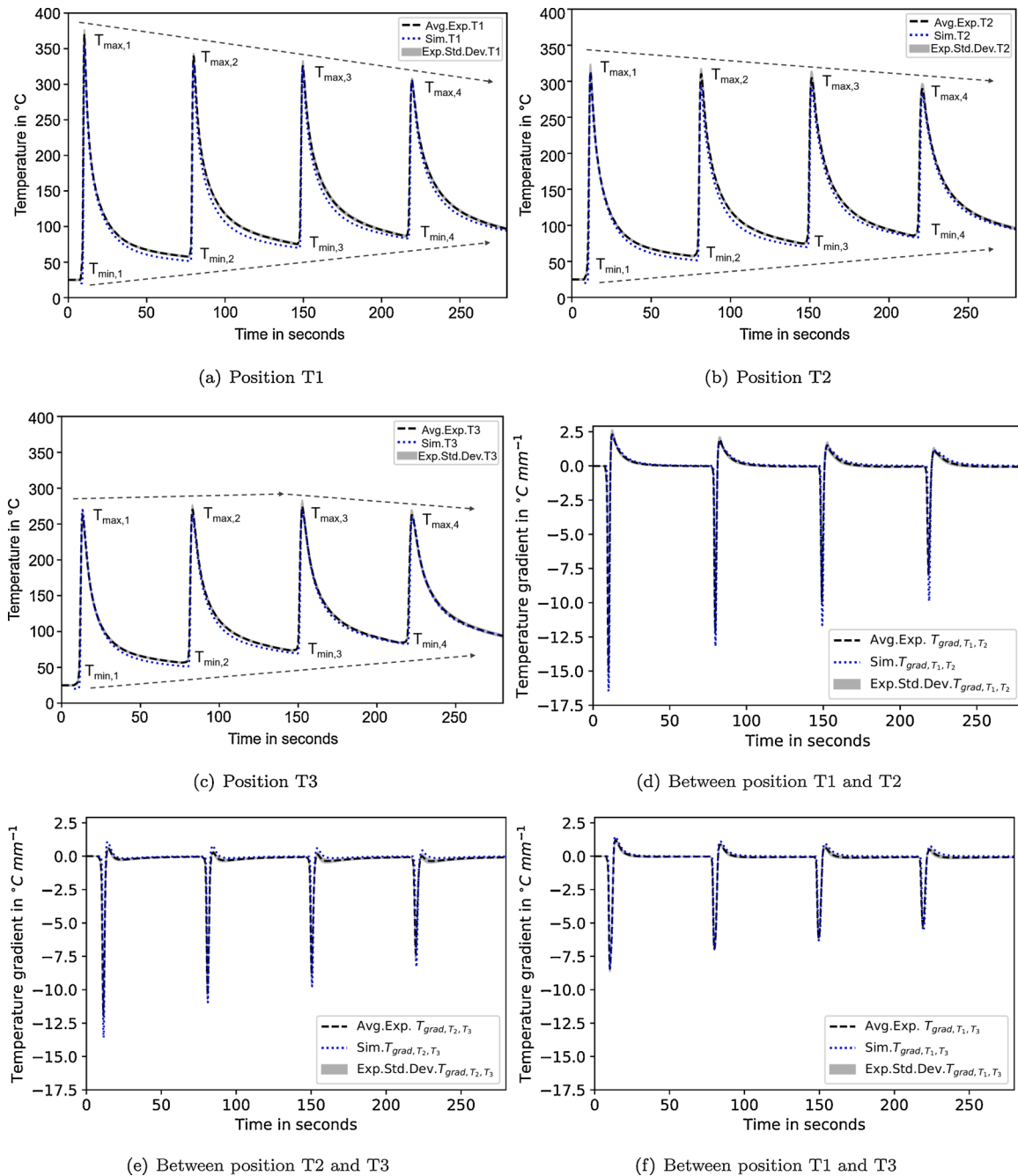
Fig. 8. Comparison of numerical (Sim.) and (average) experimental (Avg.Exp.) thermal results including experimental standard deviations (Std.Dev.): Temperatures over time at corresponding reference points T1 (a), T2 (b) and T3 (c), in addition to temperature gradients over time between T1 and T2 (d), T2 and T3 (e), as well as T1 and T3 (f) on the top substrate surface during the deposition of four layers, all showing good agreement regarding temperature maxima and minima as well as cooling behavior.

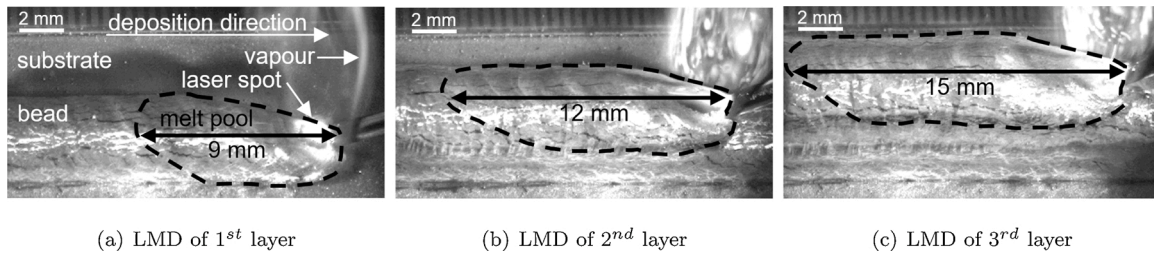(a) LMD of 1st layer

(b) LMD of 2nd layer

(c) LMD of 3rd layer

Fig. 9. Monochromatic images recorded with a high-speed camera during the deposition of the first layer (a), second layer (b) and third layer (c). The lengths of the melt pool grows from 9 mm over 12 mm to 15 mm with increasing layer numbers. Melt pool lengths were determined through image sequences and according to areas of moving reflections indicating instable surfaces above the underlying liquid melt pool.
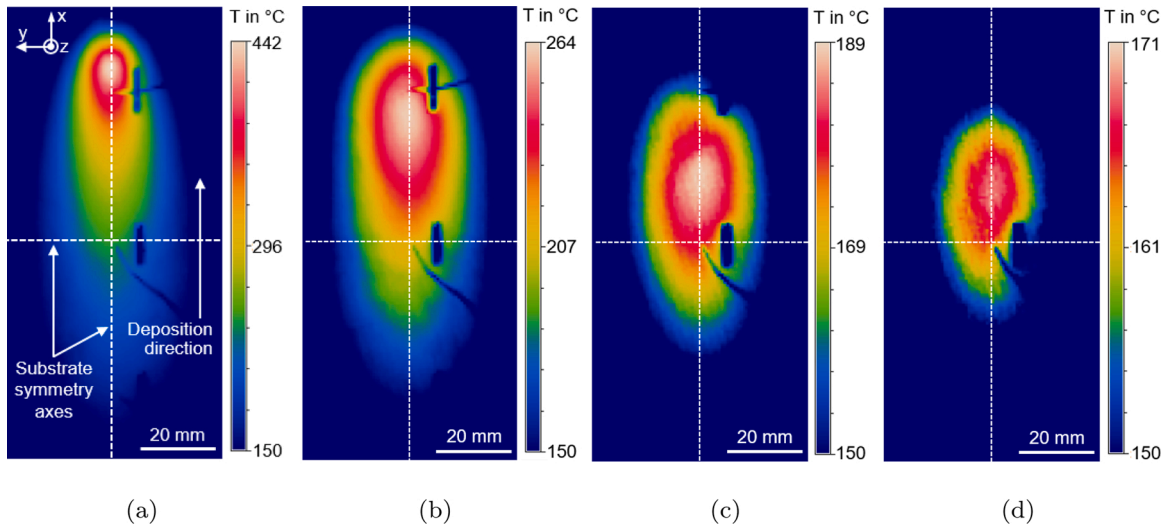

(a) (b) (c) (d)

Fig. 10. Thermographic images of bottom substrate surface after the deposition of the first layer (a) at laser switch-off, (b) after 1 s of cooling, (c) after 3 s of cooling and (d) after 4 s of cooling. The heat accumulation towards the centre of the specimen is observed. Note: The adjusted scale bar for each image to amplify the temperature differences within them.

locations of these high local stresses are correlated to the inhomogeneous temperature distribution. Local occurrences of compressive stresses appear in front of and behind the longitudinal deposition path direction. Tensile stresses are present towards the end of the deposition path, where the heat source last interacted with the material and accumulated heat is shifted towards the specimens centre during cooling. This is in agreement with typical residual stress distributions in additively manufactured wall-like structures [27,56].

The resulting distortion is provoked based on these residual stresses. Displacement results of the mechanically coupled thermal analysis of a 4-layered structure are depicted in Fig. 11(b). In the presented case, concave substrate deformation is generated in deposition direction of the structure, whereas at the edges perpendicular to the deposition direction, the deformation appear convex. Thus, the local distribution of the residual stresses and deformation strongly depend on the orientation of the deposition path. In correlation to the local heat accumulation depicted in Fig. 10, the magnitude of the distortion is higher at the end of the deposition path than at the beginning, which is in good agreement with experimental deformations of very similar specimens produced by identical process parameters by Froend et al. [15]. Overall, sequential coupling of the thermal analysis to a mechanical analysis enabled a qualitative insight into resulting residual stresses and distortions. A reduction of local temperature variations within the specimen could thus lead to a reduction in residual stresses and less deformation of the final structure [5,20]. Altogether, the numerical transient heat transfer simulation including the model calibration based on experimental identification of thermal histories and salient final-part features, such as layer geometry, was sequentially coupled to a mechanical analysis to

numerically obtained residual stresses and deformations caused by the LMD process. Hence, this model is used to perform a numerical process parameter optimization with respect to minimising residual stresses and distortion.

5. Process optimisation

For identification of process parameters and their influence on residual stresses and distortion, a sensitivity study with a number of different process conditions in the simulation has been conducted. The goal is to minimise stresses and displacements of the final part in relation to the initial parameter set that serves as a reference case. Gradual changes were made to the deposition strategy from uni-directional to bi-directional deposition direction, the inter-layer waiting time (ILWT) was gradually reduced from 60 s over 30 s to 10 s, a pre-heating temperature of the substrate of 150°C prior to the succeeding LMD at ambient air temperature of 20°C (room temperature) was investigated with ILWT of 60 s and 10 s, and the ambient air temperature during the process was increased from 20°C (room temperature) to 150°C in combination with a pre-heating temperature of the substrate of 150°C (see Table 3). All results are extracted from the model after the cooling process at room temperature.

5.1. Uni-directional vs. bi-directional deposition strategy

The deposition strategy was changed from uni-directional deposition, where the layers are deposited in the same direction with start and end points that are layer-wise superimposed, to bi-directional
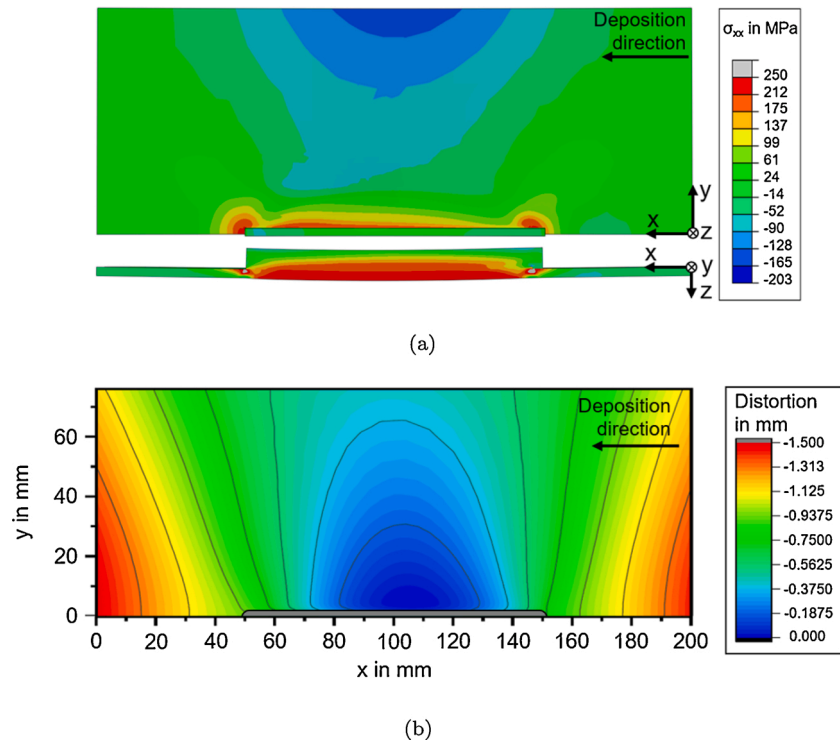
(a)

(b)

Fig. 11. Numerical model with computed results on (a) residual stresses σ_{xx} in x-direction and (b) related distortion in z-direction, both exhibiting a slight increase between the centre and end of the deposition path corresponding to the reported temperature evolution. Results represent the model after the cooling process at room temperature.

Table 3
Different parameter sets chosen for investigation of influence on residual stresses and displacements. ILWT refers to the inter-layer waiting time, which is the cooling time in between the deposition of layers. Parameters were modified in relation to the reference set (**Ref.-set**).

Sample Name	Process parameters			
	ILWT [s]	Deposition direction	Pre-heat T [°C]	Ambient T [°C]
(Ref.-set)_ILWT=60s_	60	Uni-directional	20	20
BiD(ILWT=60s)	60	Bi-directional	20	20
ILWT=30s	30	Uni-directional	20	20
ILWT=10s	10	Uni-directional	20	20
PH150(ILWT=60s)	60	Uni-directional	150	20
PH150(ILWT=10s)	10	Uni-directional	150	20
AT150(ILWT=10s)	10	Uni-directional	150	150

deposition, where the layers are deposited with alternately reversing direction. Choosing a bi-directional over an uni-directional deposition strategy led to an increase in residual stresses and displacements with the selected set of parameters, see Fig. 12. This is in agreement with results from [75]. As shown in Fig. 12(a), the σ_{xx} stresses show a constant increase of approximately 0.5% to 2% within the wall compared to uni-directional deposition. Correspondingly, increased deformation in building direction z of approximately 2.7% to 6.5% is present compared to the uni-directional deposited reference, see Fig. 12(b) and (d). This leads to the conclusion that changing from a uni-directional to a bi-directional deposition strategy within this parameter set, does not lead to a desired reduction of residual stresses and distortion and is therefore not pursued further.

5.2. Reduction of inter-layer waiting time (ILWT)

The inter-layer waiting time (ILWT) between the deposition of layers that enabled cooling of the specimen, amounted to 60 s in the initial simulation as well as during the experiments. The ILWT was incrementally reduced to 30 s and 10 s. Through this parameter change, overall displacements in building direction (z-axis) along the deposition

direction (x-axis) are reduced by 5.3% and 13.2%, respectively, see Fig. 12 (b). Hence, shorter ILWT lead to diminished structural deformation, which is in agreement with results from [76].

5.3. Pre-heating of substrate (prior to deposition)

Pre-heating the substrate to 150 °C before starting the deposition process at ambient room temperature was simulated with 60 s and 10 s ILWT. As a consequence, σ_{xx} residual stresses were further reduced by up to 3.2% for an ILTW of 60 s and up to 20.2% for an ILWT of 10 s. The σ_{yy} compressive residual stresses along the x-axis for an ILWT of 10 s were also reduced by 14.9% in front of the wall and by 10.2% in rear of the wall, see Fig. 12(c). The reductions of displacements in building direction amount to 13.6% and 31.9% along the deposition direction for 60 s and 10 s ILWT, respectively. Along the substrate-symmetry axis y, perpendicular to the deposition direction x, the drops in displacements in building direction are also significant with 22% and 30.1% for 60 s and 10 s ILWT, respectively, see Fig. 12 (d). Thus, substrate pre-heating of 150 °C lead to lower residual stresses and displacements [48].
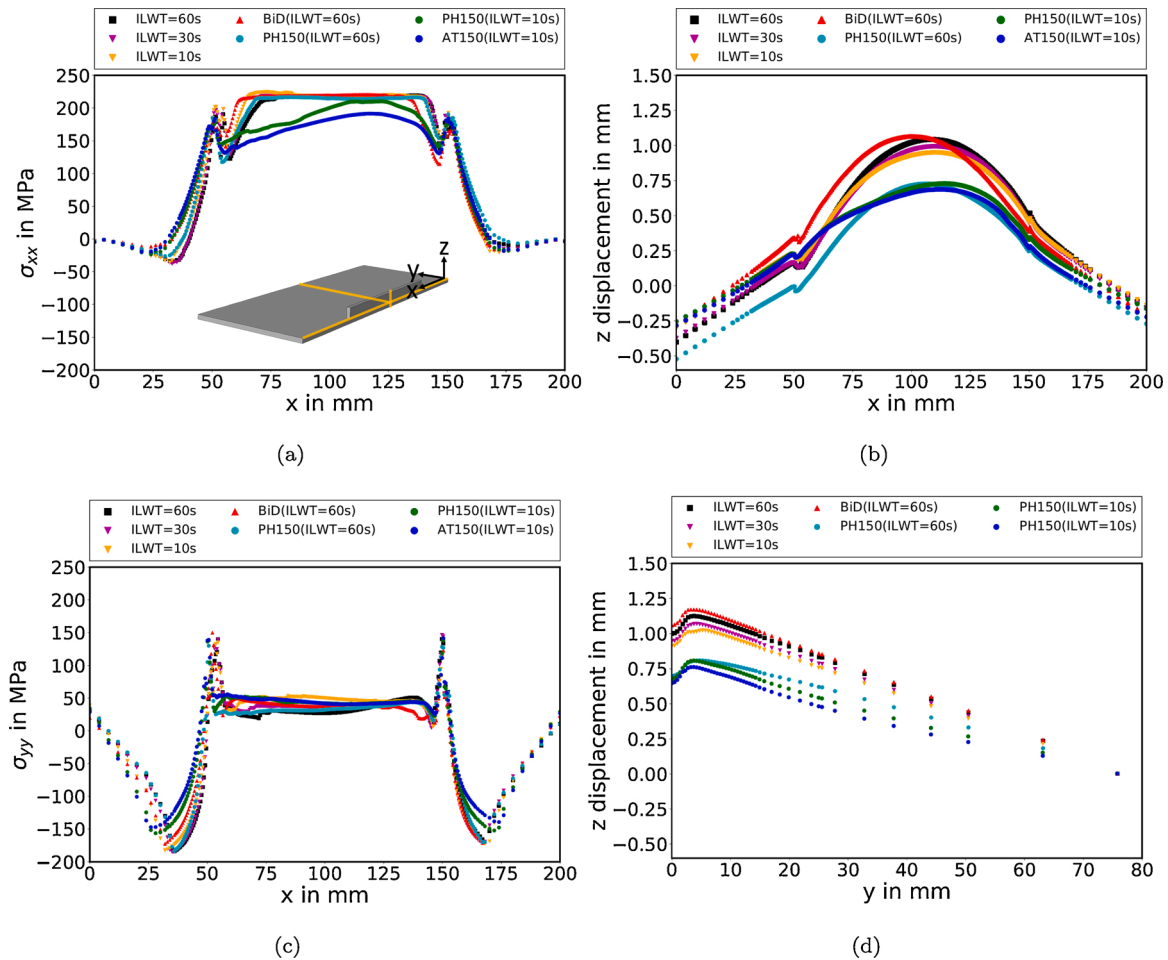
Fig. 12. Residual stress and displacement results after the cooling process at room temperature corresponding to process parameter sets of the sensitivity study listed in Table 3: (a) residual stresses σ_{xx} in and along deposition direction, (b) displacements in building direction along the deposition direction, (c) residual stresses σ_{yy} along the deposition direction, and (d) displacements in building direction along the *y*-axis perpendicular to the deposition direction.

5.4. Heating of LMD structure through ambient air temperature during deposition

Exposing the structure to an ambient air temperature of 150 °C not only prior to but also during the deposition process and keeping the inter-layer waiting time at 10 s, led to the most significant reduction in σ_{xx} of up to 27.2% along the deposition direction, see Fig. 12(a), as well as in σ_{yy} in front of the wall by 19.8% and in rear of the wall by 17.7%, see Fig. 12 (c). Accordingly, the displacements were also most significantly reduced with this parameter set by about 43%, see Fig. 12 (b), by about 32% to 48.2% along the substrate-symmetry axis *y* perpendicular to the deposition path, see Fig. 12(c). Consequently, deposition with a shorter ILWT of 10 s and heating the structure and ambient air up to 150 °C during the process, results in the most substantial decline of observed residual stresses and deformation; therefore, this combination of process parameters and conditions constitute an optimised parameter set in comparison to the initial parameter set.

6. Conclusion

In this study, an FE-model for a transient heat transfer analysis is employed to numerically calculate the temperature field during wire-based LMD processing of a 5xxx series aluminium alloy. Temperature distribution and evolution in simulation and experiment are in good agreement. Sequential mechanical coupling of the heat transfer analysis is performed to extend the model predictions to residual stresses and deformation, in order to reduce them via a model-based process

parameter optimisation. Based on the experimental and numerical results, the following findings were achieved:

- Building of the heat transfer model of the LMD process was achieved through identification of cross-sectional layer-geometries and melt pool depths, followed by a model validation through good agreement between experimental and numerically calculated temperature profiles.
- Sequential mechanical coupling of the heat transfer model enabled qualitative assessment of residual stresses and deformation.
- Application of the thermo-mechanical model to perform a parameter sensitivity study with respect to reducing final part residual stresses and deformation. The adjustments of process parameters and conditions led to the identification an optimised parameter set where the ambient temperature is increased and the inter-layer waiting time is decreased.

In summary, an efficient and powerful model was built and employed to simulate the LMD process by neglecting the microstructural evolution and melt pool dynamics. Relations between transient heat transfer, residual stresses and deformation during and after the LMD of Al-Mg were identified and utilised for process parameter optimisation. In future, the model can be used for specifying deposition strategies of more complex structures with higher layer numbers.

Declaration of interest

None.

Data availability statement

The raw/processed data can be made available upon request.

Declaration of Competing Interest

The authors report no declarations of interest.

Acknowledgements

References

[1] Dursun T, Soutis C. Recent developments in advanced aircraft aluminium alloys. Mater Des (1980–2015) 2014;56:862–71. https://doi.org/10.1016/j.matdes.2013.12.002.

[2] Schmidt M, Merklein M, Bourell D, Dimitrov D, Hausotte T, Wegener K, et al. Laser based additive manufacturing in industry and academia. CIRP Ann 2017;66(2):561–83. https://doi.org/10.1016/j.cirp.2017.05.011.

[3] Williams SW, Martina F, Addison AC, Ding J, Pardal G, Colegrove P. Wire + arc additive manufacturing. Mater Sci Technol 2016;32(7):641–7. https://doi.org/10.1179/1743284715Y.0000000073.

[4] Frazier WE. metal additive manufacturing: a review. J Mater Eng Perform 2014;23(6):1917–28. https://doi.org/10.1007/s11665-014-0958-z.

[5] Thompson SM, Bian L, Shamsaei N, Yadollahi A. An overview of direct laser deposition for additive manufacturing: Part I. Transport phenomena, modeling and diagnostics. Addit Manuf 2015;8:36–62. https://doi.org/10.1016/j.addma.2015.07.001.

[6] Zhong M, Liu W. Laser surface cladding: the state of the art and challenges. Proc Inst Mech Eng C 2009;224(5):1041–60. https://doi.org/10.1243/09544062JMES1782.

[7] Kaierle S, Barroi A, Noelke C, Hermsdorf J, Overmeyer L, Haferkamp H. Review on laser deposition welding: from micro to macro. Phys Proc 2012;39:336–45. https://doi.org/10.1016/j.phpro.2012.10.046.

[8] Huang C-Q, Deng J, Wang S-X, Liu L-L. A physical-based constitutive model to describe the strain-hardening and dynamic recovery behaviors of 5754 aluminum alloy. Mater Sci Eng A 2017;699:106–13. https://doi.org/10.1016/j.msea.2017.04.086.

[9] Hong K-M, Shin YC. Prospects of laser welding technology in the automotive industry: a review. J Mater Process Technol 2017;245:46–69. https://doi.org/10.1016/j.jmatprotec.2017.02.008.

[10] Aluminium-Taschenbuch. Düsseldorf: Aluminium-Verl; 2010.

[11] Pinkerton AJ. Lasers in additive manufacturing. Opt Laser Technol 2016;78:25–32. https://doi.org/10.1016/j.optlastec.2015.09.025.

[12] Froend M, Ventzke V, Dorn F, Kashaev N, Klusemann B, Enz J. Microstructure by design: an approach of grain refinement and isotropy improvement in multi-layer wire-based laser metal deposition. Mater Sci Eng A 2020;772:138635. https://doi.org/10.1016/j.msea.2019.138635.

[13] Klein T, Schnall M. Control of macro-/microstructure and mechanical properties of a wire-arc additive manufactured aluminum alloy. Int J Adv Manuf Technol 2020;108(1–2):235–44. https://doi.org/10.1007/s00170-020-05396-6.

[14] Wang B, Yang G, Zhou S, Cui C, Qin L. Effects of on-line vortex cooling on the microstructure and mechanical properties of wire arc additively manufactured Al-Mg alloy. Metals 2020;10(8):1004. https://doi.org/10.3390/met10081004.

[15] Froend M, Ventzke V, Riekehr S, Kashaev N, Klusemann B, Enz J. Microstructure and microhardness of wire-based laser metal deposited AA5087 using an Ytterbium fibre laser. Mater Charact 2018;143:59–67. https://doi.org/10.1016/j.matchar.2018.05.022.

[16] Yuan T, Yu Z, Chen S, Xu M, Jiang X. Loss of elemental Mg during wire + arc additive manufacturing of Al-Mg alloy and its effect on mechanical properties. J Manuf Process 2020;49:456–62. https://doi.org/10.1016/j.jmapro.2019.10.033.

[17] Derekar KS. A review of wire arc additive manufacturing and advances in wire arc additive manufacturing of aluminium. Mater Sci Technol 2018;34(8):895–916. https://doi.org/10.1080/02670836.2018.1455012.

[18] Utyaganova VR, Filippov AV, Shamarin NN, Vorontsov AV, Savchenko NL, Fortuna SV, et al. Controlling the porosity using exponential decay heat input regimes during electron beam wire-feed additive manufacturing of Al-Mg alloy. Int J Adv Manuf Technol 2020;108(9–10):2823–38. https://doi.org/10.1007/s00170-020-05539-9.

[19] Derekar K, Lawrence J, Melton G, Addison A, Zhang X, Xu L. Influence of interpass temperature on wire arc additive manufacturing (WAAM) of aluminium alloy

components. MATEC Web Conf 2019;269(7):05001. https://doi.org/10.1051/matecconf/201926905001.

[20] Shamsaei N, Yadollahi A, Bian L, Thompson SM. An overview of Direct Laser Deposition for additive manufacturing: Part II. Mechanical behavior, process parameter optimization and control. Addit Manuf 2015;8:12–35. https://doi.org/10.1016/j.addma.2015.07.002.

[21] Mackerle J. Finite element analysis and simulation of welding: a bibliography (1976–1996). Model Simul Mater Sci Eng 1996;4(5):501–33. https://doi.org/10.1088/0965-0393/4/5/006.

[22] Dal M, Fabbro R. An overview of the state of art in laser welding simulation. Opt Laser Technol 2016;78:2–14. https://doi.org/10.1016/j.optlastec.2015.09.015.

[23] Montevecchi F, Venturini G, Scippa A, Campatelli G. Finite element modelling of wire-arc-additive-manufacturing Process. Proc CIRP 2016;55:109–14. https://doi.org/10.1016/j.procir.2016.08.024.

[24] Michaleris P. Modeling metal deposition in heat transfer analyses of additive manufacturing processes. Finite Elem Anal Des 2014;86:51–60. https://doi.org/10.1016/j.finel.2014.04.003.

[25] Bock FE, Froend M, Herrnring J, Enz J, Kashaev N, Klusemann B. Thermal analysis of laser additive manufacturing of aluminium alloys: Experiment and simulation. AIP Conference Proceedings 2018;1960:140004. https://doi.org/10.1063/1.5034996.

[26] Geng H, Luo J, Li J, Gao J, Lin X. Thermal boundary evolution of molten pool during wire and arc additive manufacturing of single walls of 5A06 aluminum alloy. Metals 2020;10(7):848. https://doi.org/10.3390/met10070848.

[27] Oyama K, Diplas S, M'hamdi M, Gunnæs AE, Azar AS. Heat source management in wire-arc additive manufacturing process for Al-Mg and Al-Si alloys. Addit Manuf 2019;26:180–92. https://doi.org/10.1016/j.addma.2019.01.007.

[28] Hao M, Sun Y. A FEM model for simulating temperature field in coaxial laser cladding of TI6AL4V alloy using an inverse modeling approach. Int J Heat Mass Transf 2013;64:352–60. https://doi.org/10.1016/j.ijheatmasstransfer.2013.04.050.

[29] Farahmand P, Kovacevic R. An experimental-numerical investigation of heat distribution and stress field in single- and multi-track laser cladding by a high-power direct diode laser. Opt Laser Technol 2014;63:154–68. https://doi.org/10.1016/j.optlastec.2014.04.016.

[30] Ya W, Pathiraj B, Liu S. 2D modelling of clad geometry and resulting thermal cycles during laser cladding. J Mater Process Technol 2016;230:217–32. https://doi.org/10.1016/j.jmatprotec.2015.11.012.

[31] Tamanna N, Crouch R, Naher S. Progress in numerical simulation of the laser cladding process. Opt Lasers Eng 2019;122:151–63. https://doi.org/10.1016/j.optlaseng.2019.05.026.

[32] Liu H, Qin X, Wu M, Ni M, Huang S. Numerical simulation of thermal and stress field of single track cladding in wide-beam laser cladding. Int J Adv Manuf Technol 2019;104(9–12):3959–76. https://doi.org/10.1007/s00170-019-04056-8.

[33] Li C, Liu C, Li S, Zhang Z, Zeng M, Wang F, et al. Numerical simulation of thermal evolution and solidification behavior of laser cladding AlSiTiNi composite coatings. Coatings 2019;9(6):391. https://doi.org/10.3390/coatings9060391.

[34] Gao J, Wu C, Liang X, Hao Y, Zhao K. Numerical simulation and experimental investigation of the influence of process parameters on gas-powder flow in laser metal deposition. Opt Laser Technol 2020;125:106009. https://doi.org/10.1016/j.optlastec.2019.106009.

[35] Weisz-Patrault D. Fast simulation of temperature and phase transitions in directed energy deposition additive manufacturing. Addit Manuf 2020;31:100990. https://doi.org/10.1016/j.addma.2019.100990.

[36] Gu J, Ding J, Williams SW, Gu H, Ma P, Zhai Y. The effect of inter-layer cold working and post-deposition heat treatment on porosity in additively manufactured aluminum alloys. J Mater Process Technol 2016;230:26–34. https://doi.org/10.1016/j.jmatprotec.2015.11.006.

[37] Graf M, Hälsig A, Höfer K, Awiszus B, Mayr P. Thermo-mechanical modelling of wire-arc additive manufacturing (WAAM) of semi-finished products. Metals 2018;8(12):1009. https://doi.org/10.3390/met8121009.

[38] Abbaszadeh M, Hönnige JR, Martina F, Neto L, Kashaev N, Colegrove P, et al. Numerical investigation of the effect of rolling on the localized stress and strain induction for wire + arc additive manufactured structures. J Mater Eng Perform 2019;28(8):4931–42. https://doi.org/10.1007/s11665-019-04249-y.

[39] Hackenhaar W, Mazzaferro JA, Montevecchi F, Campatelli G. An experimental-numerical study of active cooling in wire arc additive manufacturing. J Manuf Process 2020;52:58–65. https://doi.org/10.1016/j.jmapro.2020.01.051.

[40] Li C, Yu ZB, Gao JX, Zhao JY, Han X. Numerical simulation and experimental study on the evolution of multi-field coupling in laser cladding process by disk lasers. Weld World 2019;63(4):925–45. https://doi.org/10.1007/s40194-019-00725-0.

[41] Szost BA, Terzi S, Martina F, Boisselier D, Prytuliak A, Pirling T, et al. A comparative study of additive manufacturing techniques: residual stress and microstructural analysis of CLAD and WAAM printed Ti-6Al-4V components. Mater Des 2016;89:559–67. https://doi.org/10.1016/j.matdes.2015.09.115.

[42] Wu Q, Lu J, Liu C, Fan H, Shi X, Fu J, et al. Effect of molten pool size on microstructure and tensile properties of wire arc additive manufacturing of Ti-6Al-4V alloy. Materials 2017;10(7):749. https://doi.org/10.3390/ma10070749.

[43] Miao Q, Wu D, Chai D, Zhan Y, Bi G, Niu F, et al. Comparative study of microstructure evaluation and mechanical properties of 4043 aluminum alloy fabricated by wire-based additive manufacturing. Mater Des 2020;186:108205. https://doi.org/10.1016/j.matdes.2019.108205.

[44] Bai X, Colegrove P, Ding J, Zhou X, Diao C, Bridgeman P, et al. Numerical analysis of heat transfer and fluid flow in multilayer deposition of PAW-based wire and arc additive manufacturing. Int J Heat Mass Transf 2018;124:504–16. https://doi.org/10.1016/j.ijheatmasstransfer.2018.03.085.

[45] Gu H, Li L. Computational fluid dynamic simulation of gravity and pressure effects in laser metal deposition for potential additive manufacturing in space. Int J Heat Mass Transf 2019;140:51–65. https://doi.org/10.1016/j.ijheatmasstransfer.2019.05.081.

[46] Hu R, Luo M, Liu T, Liang L, Huang A, Trushnikov D, et al. Thermal fluid dynamics of liquid bridge transfer in laser wire deposition 3D printing. Sci Technol Weld Join 2019;24(5):401–11. https://doi.org/10.1080/13621718.2019.1591039.

[47] Tran H-S, Tchuindjang JT, Paydas H, Mertens A, Jardin RT, Duchêne L, et al. 3D thermal finite element analysis of laser cladding processed Ti-6Al-4V part with microstructural correlations. Mater Des 2017;128:130–42. https://doi.org/10.1016/j.matdes.2017.04.092.

[48] Froend M, Riekehr S, Kashaev N, Klusemann B, Enz J. Process development for wire-based laser metal deposition of 5087 aluminium alloy by using fibre laser. J Manuf Process 2018;34:721–32. https://doi.org/10.1016/j.jmapro.2018.06.033.

[49] Drahntwerk Elisental W. Erdmann GmbH & Co., Aluminium filler material, supplier's material table: AA 5087. http://www.elisental.de/aluminium.php?display=tab_weld.

[50] Drahntwerk Elisental W. Erdmann GmbH & Co., Aluminium filler material, supplier's material table: AA 5754. http://www.elisental.de/aluminium.php?display=tab_weld.

[51] Zhu XK, Chao YJ. Effects of temperature-dependent material properties on welding simulation. Comput Struct 2002;80(11):967–76. https://doi.org/10.1016/S0045-7949(02)00040-8.

[52] Lindgren L-E, Runnemalm H, N”asstr“om MO. Simulation of multipass welding of a thick plate. Int J Numer Methods Eng 1999;44(9):1301–16.

[53] Andersson BAB. Thermal stresses in a submerged-arc welded joint considering phase transformations. J Eng Mater Technol 1978;100(4):356. https://doi.org/10.1115/1.3443504.

[54] Schnubel D. Laser heating as approach to retard fatigue crack growth in aircraft aluminium structures. Hamburg, Germany: Hamburg University of Technology; 2012.

[55] Mills KC. Recommended Values of Thermophysical Properties for Selected Commercial Alloys. Recommended values of thermophysical properties for selected commercial alloys. Elsevier; 2002. p. 32–6. https://doi.org/10.1533/9781845690144.211.

[56] Ding J, Colegrove P, Mehnen J, Ganguly S, Sequeira Almeida PM, Wang F, et al. Thermo-mechanical analysis of wire and arc additive layer manufacturing process on large multi-layer parts. Comput Mater Sci 2011. https://doi.org/10.1016/j.commatsci.2011.06.023.

[57] Nithiarasu P. Fundamentals of the finite element method for heat and mass transfer. Chichester, West Sussex: John Wiley & Sons Ltd; 2016. http://lib.myilibrary.com/detail.asp?ID=890233.

[58] Lindgren L-E. Computational welding mechanics: thermomechanical and microstructural simulations. Boca Raton and Cambridge, England: Woodhead Publishing in materials, CRC Press; 2007. http://search.ebscohost.com/login.aspx?direct=true&scope=site&db=nlebk&db=nlabk&AN=209505.

[59] Aluminium alloy 5754 – H22 sheet and plate. 2020. http://www.aalco.co.uk/datasheets/Aluminium-Alloy-5754-H22-Sheet-and-Plate_153.ashx.

[60] DebRoy T, David SA. Physical processes in fusion welding. Rev Mod Phys 1995;67(1):85–112. https://doi.org/10.1103/RevModPhys.67.85.

[61] Kelly SM, Kampe SL. Microstructural evolution in laser-deposited multilayer Ti-6Al-4V builds: Part II. Thermal modeling. Metall Mater Trans A 2004;35(6):1869–79. https://doi.org/10.1007/s11661-004-0095-7.

[62] Yang Q, Zhang P, Cheng L, Min Z, Chyu M, To AC. Finite element modeling and validation of thermomechanical behavior of Ti-6Al-4V in directed energy deposition additive manufacturing. Addit Manuf 2016;12:169–77. https://doi.org/10.1016/j.addma.2016.06.012.

[63] Goldak J, Chakravarti A, Bibby M. A new finite element model for welding heat sources. Metall Trans B 1984;15(2):299–305. https://doi.org/10.1007/BF02667333.

[64] Karkhin VA, Pittner A, Schwenk C, Rethmeier M. Simulation of inverse heat conduction problems in fusion welding with extended analytical heat source models. Front Mater Sci 2011;5(2):119–25. https://doi.org/10.1007/s11706-011-0137-1.

[65] Herrnring J, Staron P, Kashaev N, Klusemann B. Multiscale process simulation of residual stress fields of laser beam welded precipitation hardened AA6082. Materialia 2018;3:243–55. https://doi.org/10.1016/j.mtla.2018.08.010.

[66] Chiumenti M, Cervera M, Salmi A, Agelet de Saracibar C, Dialami N, Matsui K. Finite element modeling of multi-pass welding and shaped metal deposition processes. Comput Methods Appl Mech Eng 2010;199(37–40):2343–59. https://doi.org/10.1016/j.cma.2010.02.018.

[67] Costa L, Vilar R, Reti T, Deus AM. Rapid tooling by laser powder deposition: process simulation using finite element analysis. Acta Mater 2005;53(14):3987–99. https://doi.org/10.1016/j.actamat.2005.05.003.

[68] Lundbäck A. Modelling and simulation of welding and metal deposition. Luleå: Luleå University of Technology; 2010 [Doctoral thesis].

[69] D'Ostuni S, Leo P, Casalino G. FEM simulation of dissimilar aluminum titanium fiber laser welding using 2D and 3D Gaussian heat sources. Metals 2017;7(8):307. https://doi.org/10.3390/met7080307.

[70] Lu X, Lin X, Chiumenti M, Cervera M, Hu Y, Ji X, et al. Residual stress and distortion of rectangular and S-shaped Ti-6Al-4V parts by directed energy deposition: modelling and experimental calibration. Addit Manuf 2019;26:166–79. https://doi.org/10.1016/j.addma.2019.02.001.

[71] Froend M, Ventzke V, Kashaev N, Klusemann B, Enz J. Thermal analysis of wire-based direct energy deposition of Al-Mg using different laser irradiances. Addit Manuf 2019;29:100800. https://doi.org/10.1016/j.addma.2019.100800.

[72] Radaj D. Welding residual stresses and distortion: calculation and measurement. rev. ed. Düsseldorf: DVS-Verl; 2003.

[73] Masubuchi K. Analysis of welded structures: residual stresses, distortion, and their consequences. Elsevier; 1980. https://doi.org/10.1016/C2013-0-05818-5.

[74] Biegler M, Graf B, Rethmeier M. In-situ distortions in LMD additive manufacturing walls can be measured with digital image correlation and predicted using numerical simulations. Addit Manuf 2018;20:101–10. https://doi.org/10.1016/j.addma.2017.12.007.

[75] Lee Y, Bandari Y, Nandwana P, Gibson BT, Richardson B, Simunovic S. Effect of interlayer cooling time, constraint and tool path strategy on deformation of large components made by laser metal deposition with wire. Appl Sci 2019;9(23):5115. https://doi.org/10.3390/app9235115.

[76] Heigel JC, Michaleris P, Reutzel EW. Thermo-mechanical model development and validation of directed energy deposition additive manufacturing of Ti-6Al-4V. Addit Manuf 2015;5:9–19. https://doi.org/10.1016/j.addma.2014.10.003.